

NO₂ Quantum Yield from the 248 nm Photodissociation of Peroxynitric Acid (HO₂NO₂)

Coleen M. Roehl¹, Troy L. Mazely², Randall R. Friedl, Yumin Li³, Joseph S. Francisco³
and Stanley P. Sander*

*Jet Propulsion Laboratory, California Institute of Technology, 4800 Oak Grove Drive,
Pasadena, CA 91109*

¹present address: Division of Geological and Planetary Sciences, California Institute of Technology, Pasadena, CA 91125

²present address: Science Applications International Corporation, 21151 Western Ave, Torrance, CA 90501

³Department of Chemistry and Department of Earth and Atmospheric Sciences, Purdue University, West Lafayette, IN 47907-1393

* Also with the Division of Geological and Planetary Sciences, and Division of Engineering and Applied Science, California Institute of Technology, Pasadena, CA 91125. Author to whom correspondence should be addressed.
email: ssander@jpl.nasa.gov fax: (818) 393-5019. address: M/S 183-901, Jet Propulsion Laboratory, 4800 Oak Grove Dr., Pasadena, CA 91109

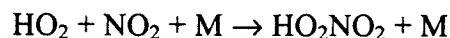
Abstract

Peroxynitric acid (PNA) was photolyzed at 248 nm and the NO₂ photoproduct was detected by laser induced fluorescence (LIF). The quantum yield for the production of NO₂ was determined by comparison with HNO₃ photolysis data taken under identical experimental conditions. Measurements made over a range of pressures, flows, and precursor concentrations resulted in an NO₂ quantum yield of 0.56 ± 0.09 , where the statistical uncertainty is 2 standard deviations. Calculations of potential energy curves for several low-lying singlet and triplet states of PNA are presented. The calculations show that while the singlet excitations occur via an $n-\pi^*$ transition on the NO₂ moiety, the dissociative channels forming OH + NO₃ and HO₂ + NO₂ likely occur via predissociation on different surfaces. Excitation energies at the MRCI and CCSD(T) level of theory show that excited states of PNA are accessible at wavelengths longer than 407 nm (~ 3.0 eV).

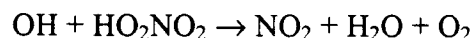
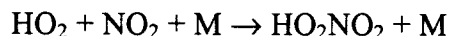
Submitted to the Journal of Physical Chemistry, Harold Johnston Festschrift

Introduction

Investigations of the atmospheric impacts of aircraft emissions ^{1,2}, industrial and agricultural emissions ³ and changes in the radiative balance of the atmosphere ⁴ invariably focus on the chemical mechanisms which control the production and loss of ozone. These mechanisms are strongly influenced by species which couple the members of different chemical families. An example is peroxyxynitric acid, HO₂NO₂, which couples odd hydrogen (HO_x) and odd nitrogen (NO_x) in the upper troposphere and lower stratosphere. PNA is formed by the recombination reaction,

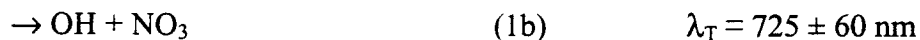


and removed mainly by reaction with OH, photolysis and thermal decomposition. PNA plays a key role in the destruction of HO_x radicals by the catalytic cycle:

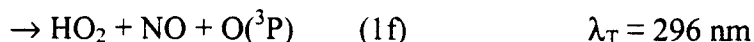
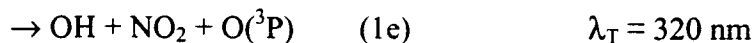


PNA also acts as a temporary reservoir for HO_x and NO_x radicals.

Atmospheric models currently consider two PNA photodissociation pathways:



where the threshold wavelengths are derived from thermodynamic data at 298 K ⁵. The atmospheric modeling community uses values of 0.67 and 0.33 for the quantum yields for channels 1a and 1b, respectively, over the entire ultraviolet spectrum of PNA. Other photodissociation channels and their thresholds are:



Although there have been a number of measurements of PNA cross sections in the UV ⁶⁻¹⁰, relatively little work has been carried out on photodissociation quantum yields. The only study is that of MacLeod *et al.* who measured the quantum yield for OH formation from PNA photolysis at 248 nm ¹¹. In the latter study, the OH product yield from PNA photolysis was measured relative to that from H₂O₂ in a very low pressure photolysis reactor / mass spectrometer system. A quantum yield of 34±16% was determined for the production of OH radicals, implying a quantum yield of roughly 66% for the NO₂ + HO₂ product channel. Difficulty in measuring absolute, unambiguous PNA concentrations by mass spectrometry complicated their results.

The weak HO₂-NO₂ bond in PNA results in a photodissociation threshold which lies in the near-infrared and can be broken by a process mediated by overtones and combination bands involving the O-H stretching mode ^{12,13}. This mechanism has been invoked to explain the observed dependence of OH and HO₂ at high solar zenith angles in the lower stratosphere ¹⁴. While cross sections of the second and third overtone bands (3v₁ and 4v₁) have been measured recently in solution ¹⁵ and gas phase ¹⁶ there are as yet no photodissociation quantum yield measurements for these or other infrared bands.

In this study, PNA was photolyzed at 248 nm and NO₂ photoproduct was detected by laser induced fluorescence (LIF). PNA vapor concentrations were calculated from on-line ultraviolet (UV) absorption measurements. The NO₂ quantum yield from PNA was determined by comparison to HNO₃ photolysis data taken under identical experimental conditions. The quantum yield was investigated as a function of total flow rate and total pressure over a range of precursor concentrations. Similar photolysis experiments with HNO₃ and PAN have been performed in this lab. ¹⁷⁻¹⁹ The experimental results are complemented by calculations of the ground and excited state potential surfaces which help to rationalize the measured quantum yield.

Experimental Section

The apparatus used in this study has been thoroughly described in previous publications, ¹⁷⁻¹⁹ and hence only a brief description along with the slight modifications and particular experimental conditions will be discussed here. A diagram of the apparatus is shown in Figure 1. Gaseous PNA or HNO₃ was introduced into a flowing system by passing a calibrated Ar flow

through either a PNA or HNO_3 sample, which was contained in a quartz reservoir placed in an ice bath. Ar was chosen as the carrier gas because of its relatively slow diffusivity and low fluorescence quenching efficiency. The pressure in the reservoirs (30 – 100 Torr) was adjusted using a Teflon needle valve located between the reservoirs and a quartz photolysis cell and was monitored with a 100 Torr MKS Baratron capacitance manometer. Typical Ar flows through the reservoirs were 30 – 100 sccm. Also located upstream of the needle valve were two bypass cells (5 and 30 ± 0.1 cm in length) used during UV absorption measurements. The precursor gases were further diluted with Ar in a mixing volume downstream of the needle valve and before entering the photolysis cell. The partial pressure of the precursors was maintained low enough so that the fluorescence quenching was dominated by the Ar carrier gas. The residence time in the photolysis cell was adjusted by varying the total flow rates between 500 - 1400 sccm and the photolysis cell pressure, which was maintained at 3.0, 7.0, or 10.0 Torr. These conditions ensured that the NO_2 photoproduct was removed from the detector viewing zone between excimer pulses.

An excimer laser operated at 248 nm with an energy density of 75 mJ/cm^2 and at a repetition rate of 30 Hz was used to photolyze the PNA and HNO_3 precursors. The weakly focused excimer beam entered and exited the photolysis cell through quartz windows located perpendicular to flow of gas and attached to the body of the photolysis cell by o-ring joints. By separating the windows from the cell body with o-ring joints and adding blackened baffles in the extended side arms of the photolysis cell, the fluorescence background induced by the excimer laser was reduced. A portion of pure carrier gas flow was directed through the side arms to keep the dead volume flushed during measurements. Typically 16,000 laser shots were averaged for one experiment (approx. 10 minutes).

The 511 nm line of a 10 kHz pulsed copper vapor (probe) laser with ~2 Watts of power was utilized for LIF detection of NO_2 . Light emitted from the copper vapor laser was passed through two dichroic filters, to eliminate the 578 nm line of the copper vapor laser, and telescoping optics, to reduce the beam diameter to about 0.5 cm, before entering the photolysis cell. The high repetition frequency of the probe laser allowed for the acquisition of LIF data points every 100 μs .

Fluorescence from the excited NO_2 was detected by a cooled photomultiplier tube (PMT: Burle C31034-02) that was oriented perpendicular to the laser beam axes. Collection optics served to focus the light onto the cathode of the PMT. Blackened baffles lining the housing tube leading to the PMT and a quartz window (rather than Pyrex) were utilized to reduce undesirable background fluorescence from the excimer laser and scattered light. A 3.8 cm long quartz cell, filled with 0.36 M $\text{K}_2\text{Cr}_2\text{O}_7$ and containing an aluminum honeycomb baffle, were used to filter out scattered light below about 530 nm. Finally, a 578 nm notch filter selectively eliminated any residual Cu vapor emission at that wavelength. The LIF signal was amplified, discriminated, and counted with a multichannel scalar card configured with 10 μs bin widths, and stored on a PC.

Nitric acid was prepared by collecting the vacuum distillate of a 50:50 by volume mixture of 95% H_2SO_4 with NaNO_3 . The HNO_3 was maintained at 0 °C by placing the sample in an ice bath. Peroxynitric acid was synthesized by the reaction of H_2O_2 (>90%) with NO_2BF_4 using the procedure described by Kenley *et al.*²⁰ 90% H_2O_2 was prepared by a vacuum distillation of 70% Semiconductor Grade H_2O_2 (FMC Corporation) and gravimetric techniques were used to verify the percent composition.

The PNA synthesis method of Kenley *et al.* produces several impurities that must be removed and/or quantified by careful analysis before use in photodissociation experiments. The spectra of a number of different PNA samples were obtained off-line from the photodissociation experiment using mid-infrared Fourier transform infrared (FTIR) and near-infrared long-path absorption/diode array spectrometer techniques. PNA fundamental vibrational bands ($\nu_2 - \nu_7$) as well as bands from HNO_3 , SiF_4 , H_2O_2 , H_2O , and NO_2 impurities were identified in the mid-IR spectra, and HNO_3 , H_2O_2 , H_2O overtone bands, and NO_2 electronic bands were identified in the near-IR spectra¹⁶. Compositions of the samples were determined using literature values of cross sections and band strengths for both spectral regions.^{21,22,16} The dependence of the impurity levels as a function of the PNA sample age has been discussed by Li *et al.*²³ and Zhang *et al.*¹⁶ who found that both NO_2 and HNO_3 decreased with time due to fractional distillation. In the present work it was found that the ratio $[\text{PNA}]/[\text{HNO}_3]$ was ~10-33 while the ratio $[\text{PNA}]/[\text{H}_2\text{O}_2]$ ranged from ~0.5-5. The NO_2 band centered near 1600 cm^{-1} was observed in spectra of freshly made samples, but decreased rapidly after several minutes of bubbling. No

attempt was made to quantify this impurity. The SiF₄ and H₂O impurities were not quantified since they do not absorb in the UV and hence could not interfere with the on-line UV absorption measurements (discussed below) nor do they interfere with the quantum yield determinations.

Concentrations of PNA and HNO₃ in the photolysis cell were determined immediately before and/or after every photolysis experiment by passing the gas flows through parallel 5 and 30 cm long UV absorption cells upstream of the photolysis cell. UV absorption measurements were made at two wavelengths 214 nm (Zn lamp, 5 cm cell) and 254 nm (Hg Pen Ray lamp, 30 cm cell) and then were used along with calibrated flow rates and the Beer-Lambert Law to calculate vapor concentrations in the photolysis cell. Vapor concentrations obtained at the two wavelengths were compared and averaged. In the HNO₃ photolysis experiments, vapor pressures inferred from the photometric measurements were always within several percent of each other and typically in the range of 13.5 – 14.5 torr, in excellent agreement with known vapor pressures for pure HNO₃ at 0° C.²⁴ In the PNA photolysis experiments, the photometric measurements provided a way to measure the fractional impurity of HNO₃. This is possible because there is a

significant difference in the ratio $\frac{\sigma_{\text{PNA}}^{\lambda}}{\sigma_{\text{HNO}_3}^{\lambda}}$ at $\lambda = 254$ nm and 214 nm (the values are 18 and 4.1, respectively). It was found that the vapor pressure of the PNA samples varied over the range 0.3-1.0 Torr depending on the age of the sample. Differences in the PNA concentrations obtained at the two wavelengths were usually less than 10% and samples with concentrations differing by more than 20% (implying a significant HNO₃ impurity) were discarded. Unlike HNO₃, the H₂O₂ impurity in the PNA sample could not be checked in the on-line UV absorption cells because the

ratio $\frac{\sigma_{\text{PNA}}^{\lambda}}{\sigma_{\text{H}_2\text{O}_2}^{\lambda}}$ does not differ significantly between 254 and 214 nm (5.4 and 5.8, respectively). The infrared spectra provided a means for estimating the H₂O₂ impurity as a function of sample age, and new PNA samples were produced when the measured PNA vapor pressure dropped by 50%. Since H₂O₂ photolysis at 248 nm has no effect on the NO₂ signal, the primary effect of H₂O₂ impurity is to introduce a small error in the determination of [PNA].

After further dilution, the concentration ranges of photolyte in the PNA and HNO₃ photolysis experiments were $(1 - 43) \times 10^{13} \text{ cm}^3$ and $(2 - 23) \times 10^{14} \text{ cm}^3$, respectively.

Computational Methods

The ground state of HO_2NO_2 was optimized at the CCSD(T) level of theory²⁵ with the cc-pVDZ basis set.²⁶ At the optimized geometry of the ground state, the vertical excitation energies for the lowest two singlet excited states, 2^1A and $3^1\text{A}'$, and the lowest two triplet excited states, 1^3A and 2^3A , are calculated at the CASSCF^{27,28} and MRCI^{29,30} level of theory with the cc-pVDZ basis set. The potential energy curves for the 1^1A , 2^1A , and 3^1A states are calculated at the CASSCF level of theory with the cc-pVDZ basis set along the $R_{\text{O-O}'}$, $R_{\text{O'-N}}$ and $R_{\text{N-O}'}$ coordinates, separately, while fixing other parameters at their equilibrium values of the ground state.

The active space used for the CASSCF calculation in this work is (16e,11mo) which includes eight doubly-occupied molecular orbitals and three virtual molecular orbitals. The size of the CAS in this active space is 9075 CSFs (configuration state functions) for the singlet states and 13068 CSFs for the triplet states.

Results

Temporal fluorescence data following the photolysis of PNA and HNO_3 were collected over a range of concentrations, pressures and flow rates in 10 μs bins. Background noise from cell and filter fluorescence induced by the excimer laser, which decays more rapidly than the LIF signal, was easily deduced from data collected between probe pulses and was subtracted from these raw data. The residual LIF signal consisted of 1) NO_2 generated from PNA or HNO_3 photolysis, 2) NO_2 from PNA or HNO_3 decomposition, and 3) probe laser scatter through the optical and chemical filters. These temporal profiles were collected until the NO_2 photoproduct completely left the detection viewing zone, at which time the LIF signal was constant and solely resulted from processes 2 and 3 above. The fluorescence signal from the PNA photofragment was calculated by subtracting this constant background signal. Typical curves generated from the photolysis of PNA for 3.0, 7.0, and 10.0 Torr total pressure are illustrated in Figure 2(a-c), respectively. Similar plots were obtained for HNO_3 photolysis in experiments performed immediately before or after the PNA measurements.

The temporal fluorescence signals such as those shown in Figure 2 are proportional to the NO₂ concentrations present at a particular time after the photolysis pulse and can be related to the NO₂ quantum yield (from PNA or HNO₃ photolysis) by the following equation:

$$[\text{NO}_2]_i = \Lambda \phi_i^{\text{NO}_2}(\lambda_{\text{photo}})[i]\sigma_i(\lambda_{\text{photo}}) \quad (2)$$

where Λ is a detector response function, $\phi_i^{\text{NO}_2}$ is the NO₂ quantum yield of the precursor, i , which has an initial concentration, $[i]$, and an optical cross section, $\sigma_i(\lambda_{\text{photo}})$ at the photolysis wavelength, λ_{photo} . To avoid the difficulty in having to directly determine Λ , HNO₃ is used as a calibrant. By measuring the NO₂ LIF signals from back-to-back experiments with PNA and HNO₃ precursors, the detector response function is eliminated, i.e.

$$\frac{[\text{NO}_2]_{\text{PNA}}}{[\text{NO}_2]_{\text{HNO}_3}} = \frac{S_{(\text{PNA})}(\tau)}{S_{(\text{HNO}_3)}(\tau)} = \frac{\phi_{\text{PNA}}^{\text{NO}_2}(\lambda_{\text{photo}})}{\phi_{\text{HNO}_3}^{\text{NO}_2}(\lambda_{\text{photo}})} \frac{[\text{PNA}]}{[\text{HNO}_3]} \frac{\sigma_{\text{PNA}}(\lambda_{\text{photo}})}{\sigma_{\text{HNO}_3}(\lambda_{\text{photo}})} \quad (3)$$

$S_i(\tau)$ is the fluorescence signal from each of the precursors at time, τ , after photolysis. Since HNO₃ photodissociates at 248 nm to produce NO₂ product with a quantum yield of unity¹⁸, Equation 3 can be rewritten as:

$$\phi_{\text{PNA}}^{\text{NO}_2}(\lambda_{\text{photo}}) = \phi_{\text{HNO}_3}^{\text{NO}_2}(\lambda_{\text{photo}}) \frac{S_{\text{PNA}}(\tau)}{S_{\text{HNO}_3}(\tau)} \frac{[\text{HNO}_3]}{[\text{PNA}]} \frac{\sigma_{\text{HNO}_3}(\lambda_{\text{photo}})}{\sigma_{\text{PNA}}(\lambda_{\text{photo}})} \quad (4)$$

The recommended cross sections⁵, $\sigma_{\text{HNO}_3}(248 \text{ nm}) = 2.00 \times 10^{-20} \text{ cm}^2 \text{ molecule}^{-1}$ and $\sigma_{\text{PNA}}(248 \text{ nm}) = 4.58 \times 10^{-19} \text{ cm}^2 \text{ molecule}^{-1}$ were used to obtain $\phi_{\text{PNA}}^{\text{NO}_2}$. In order to determine the relative production of NO₂ from each precursor, the time-dependent fluorescence signals from both HNO₃ and PNA were ratioed and averaged at set delays between the photolysis and probe pulses. This ratio of independent values gives the relative yield of NO₂, $S_{\text{PNA}}(\tau)/S_{\text{HNO}_3}(\tau)$, for Eq.4. This procedure was repeated for all sets of data. The results of the measurements made at total flows $\geq 700 \text{ sccm}$ are plotted versus the ratio of the precursor concentrations in Figure 3. Results for flows $< 700 \text{ sccm}$ were not used as discussed in the next section. Each data point represents a temporally averaged ratio of LIF signals. The vertical error bars were determined by the

statistical error in the signal ratio, while the horizontal error bars were dominated by the uncertainty in the PNA concentration measurement. The line represents the linear regression of these data points and has a slope = $S_{\text{PNA}}(\tau)/S_{\text{HNO}_3}(\tau) \times [\text{HNO}_3]/[\text{PNA}] = 12.3 \pm 1.0$. Substituting this value and the PNA and HNO_3 concentrations calculated from the UV absorption measurements into Equation 4 results in a quantum yield of 0.56 ± 0.09 for the production of NO_2 from PNA photolysis at 248 nm. The results of all data sets are tabulated in Table 1.

Discussion

As stated above, the quantum yield of NO_2 production from PNA photolysis was determined by solving Equation 4 using LIF data collected over a variety of PNA and HNO_3 concentrations at total flow rates greater than 700 sccm and at total pressures of 3.0, 7.0, and 10.0 Torr. Results shown in Figure 2 appear to be independent of total pressure and linear over the concentration ranges chosen. This is in contrast to LIF data collected at similar pressures and flows of 500 sccm, which exhibited a marked pressure dependence (see Table 1). This dependence is attributed to decomposition of PNA on the walls as results of the longer residence times.

Evidence of diffusion, fluorescence quenching, and collisional deactivation of the internally excited nascent NO_2 photoproduct is seen in the LIF profiles (Figure 2) at short time scales. Similar profiles were obtained in the earlier studies with HNO_3 and PAN.¹⁷⁻¹⁹ At total pressures of 3.0 Torr, the vibrational relaxation of NO_2 was not completed before the first LIF data was recorded and hence there is an observable initial growth in the LIF signal. This growth is much less pronounced in the 7.0 Torr data and is not detectable by 10.0 Torr. Fluorescence quenching is more efficient at 10.0 Torr total pressure, however, so the maximum signal for comparable PNA or HNO_3 concentrations is less than that at lower pressures. For measurements conducted at constant flow rates, but varying total pressures (such as those in Figure 2), the effects of diffusion out of the viewing zone can be detected. The fluorescence decay at 3.0 Torr is more rapid than at 10.0 Torr due to the faster diffusion and decreased residence time in the photolysis cell.

Finally, we report a quantum yield for the production of NO_2 from PNA photolysis of 0.56 ± 0.09 . This is somewhat lower than the value inferred from the results of MacLeod *et al.*

¹¹, but is within the stated errors and can be considered to be in agreement considering the complexity of the reaction mechanism invoked to interpret the measurements of MacLeod *et al.*

¹¹ The most difficult part of the earlier study was associated with characterizing the purity and amounts of PNA using mass spectrometric techniques. This problem was circumvented, in part, in this study by measuring the vapor concentrations in situ via UV absorption and by incorporating the results from off-line FTIR and the near IR experiment. Another consideration in this regard is that the current work and the MacLeod *et al.* study may be influenced by dissociation of hot photofragments. In this study, NO₂ can be formed from the decomposition of excited NO₃ (channel 1e) and removed by decomposition of excited NO₂ (channel 1f). The measurement of OH in the MacLeod *et al.* work may be influenced by the decomposition of excited HO₂ (channel 1e). These effects may be responsible for the failure of the observed OH and NO₂ quantum yields to sum to unity at 248 nm. Both experiments, however, measure the quantities that are important for the purposes of atmospheric modeling.

Calculations of Potential Energy Surfaces. The optimized geometry of the HO₂NO₂ ground state is shown in Figure 4. The optimized results of calculations at the CCSD(T)/cc-pVDZ level of theory indicate that the ground state of HO₂NO₂ has no symmetry and that all the heavy atoms lie approximately in one plane. The electronic configurations for the singlet and triplet states in this study are summarized in Table 2. The configuration of the ground state is

$$(\text{core})^{10}(1-17)a^218a^219a^220a^221a^022a^023a^0.$$

The core consists of molecular orbitals formed by the 1s orbitals of the five heavy atoms. 18a is a non-bonding molecular orbital with contributions from the 2p orbitals of the two oxygen atoms of NO₂ and lies approximately perpendicular to the molecular plane. The 19a and 20a molecular orbitals are the non-bonding molecular orbitals consisting mainly of the 2p orbitals of the two oxygen atoms in the NO₂ group. These orbitals lie in the heavy atom plane. The 21a orbital is the π -type anti-bonding MO formed from the 2p orbitals of the two oxygen atoms and the nitrogen atom of the NO₂ group, and is perpendicular to the heavy atom plane. The excited states, 2¹A, 3¹A, 1³A, and 2³A, are derived from the single electronic transitions 20a \rightarrow 21a, 19a \rightarrow 21a, 18a \rightarrow 21a, and 20a \rightarrow 21a, separately. The excited states studied in this work can be described as n \rightarrow π^* transitions on the NO₂ group.

As shown in Table 3, the vertical excitation energy for the 2^1A state is 5.05 eV (246 nm). This is somewhat smaller than the value of 5.823 eV (5.610 eV with electron correlation) obtained by Saxon and Liu using the CI singlet method with the DZP basis set ³¹. Recently, Chen and Hamilton calculated the vertical excitation energies of the lowest singlet state to be 5.041 and 4.903 eV with CAS and CASPT2 wavefunctions, respectively, using the B3LYP/6-31G* geometry. ³² Our results are consistent with both the CAS and CASPT2 results of Chen and Hamilton. The present results are also consistent with the presence of a small feature in the absorption spectrum at 250 ± 10 nm (4.97 eV).

The potential energy curves calculated for the three singlet states along the $R_{O-O'}$, $R_{N-O'}$ and $R_{N-O''}$ coordinates are shown in Figure 5(a-c). As can be seen in Figure 5a, the lowest singlet excited states, 2^1A and 3^1A are weakly bound along the $R_{O-O'}$ coordinate in the Franck-Condon region, but their potential energy curves show curve crossing which could lead to predissociation as a result of the intersection with other unbound states. Along the $R_{N-O'}$ coordinate, the potential energy curve for the 2^1A state is shallower than the curve for the $R_{O-O'}$ coordinate in the Franck-Condon region and intersects with other unbound states leading to predissociation. The 3^1A state is bound and also intersects with other unbound states around the Franck-Condon region. Along the $R_{N-O''}$ coordinate, the potential energy curves of the 2^1A and 3^1A states are more strongly bound in the Franck-Condon region than those along the . This is because the relevant electronic transition, $n \rightarrow \pi^*$, is located primarily on the NO_2 moiety. Also, the crossings between the 2^1A and 3^1A states and the repulsive states occur at larger values of internuclear separation on the N-O' coordinate compared with the crossings that occur on the O-O'' and N-O'' coordinates.

The calculated potential energy curves in Figure 5 provide a way to rationalize the observed PNA photolysis quantum yields. At 248 nm, HO_2NO_2 dissociation through the NO_2 moiety is unfavorable because there is no curve crossing in the Franck-Condon region along the $R_{N-O'}$ coordinate for the 2^1A excited state. There is curve crossing in the Franck-Condon region for the weakly bound 2^1A state along the $R_{O-O'}$ coordinate, and any leakage could predissociate along the $R_{O-O'}$ coordinate to produce $OH + NO_3$. There is curve crossing in the Franck-Condon

region for the 2^1A state along the R_{N-O^*} coordinate which leads to the formation of $HO_2 + NO_2$ by predissociation. Comparing Figure 5a and Figure 5b we can see that photodissociation yields along the R_{N-O^*} coordinate should be greater than along the R_{O-O^*} coordinate because the O^*-O surface is shallower and curve crossing occurs at smaller internuclear separations. This is consistent with the observed quantum yields of 0.34 for OH formation¹¹ and 0.56 for NO_2 formation at 248 nm.

The vertical excited state energies of the triplet states are summarized in Table 3. The two lowest triplet states are found to lie below the lowest excited singlet state. The energy of the lowest triplet state is estimated to be 4.26 eV. The next triplet state lies about 0.5 eV above the 1^3A state. The triple excited states all have predominantly valence character. Both the triplet states of HO_2NO_2 involve promotion into an orbital with anti-bonding character in the NO_2 chromophore, as is the case for the corresponding second and third singlet excited states. To obtain a better understanding of the band origin of the lowest triplet state, the geometry of this states was optimized at the CCSD(T)/cc-pVDZ level of theory. The results for the optimized ground state and lowest triplet state are presented in Table 4. These results show that there is significant internal rotation that occurs around the NO bond (HOO^*-NO_2). There is also a significant lengthening of the NO bonds on the NO_2 group. These changes are consistent with the reduction in bond order associated with the $n \rightarrow \pi^*$ transition for this state. A recent *ab initio* study of HO_2NO_2 calculated at the MP2(Fc)/6-311++G** level by Jitariu and Hirst³³ shows similar trends in structural changes in the NO_2 group upon excitation into the triplet state. The singlet-triplet (S_0-T_1) splitting calculated in this study is 3.26 eV. This compares with a value of 3.04 eV calculated by Jitariu and Hirst using the G2MP2 method³³. These results imply that the origin of the singlet-triplet absorption starts around 407 nm.

Acknowledgement

This paper is dedicated to Harold S. Johnston whose many contributions to kinetics and photochemistry have made a major impact on both atmospheric chemistry and public policy. We

would like to acknowledge the technical support of Mr. Dave Natzic. The supercomputer used in this investigation was provided by funding from the NASA Offices of Earth Science, Aeronautics and Space Science. The research was carried out by the Jet Propulsion Laboratory, California Institute of Technology, under contract with the National Aeronautics and Space Administration.

References

- (1) Johnston, H. S.; Kinnison, D. E.; Wuebbles, D. J. *J. Geophys. Res.* **1989**, *94*, 16351-16364.
- (2) *Aviation and the Global Atmosphere*; Penner, J. E.; Lister, D. H., Eds.; Cambridge University Press: Cambridge, 1999.
- (3) *WMO Scientific Assessment of Ozone Depletion: 1998*; World Meteorological Organization: Geneva, 1999.
- (4) *IPCC Climate Change 1995*; Cambridge University Press: Cambridge, 1996.
- (5) DeMore, W. B.; Sander, S. P.; Golden, D. M.; Hampson, R. F.; Kurylo, M. J.; Howard, C. J.; Ravishankara, A. R.; Kolb, C. E.; Molina, M. J. "Chemical Kinetics and Photochemical Data for Use in Stratospheric Modeling, Evaluation Number 12," Jet Propulsion Laboratory, California Institute of Technology, 1997.
- (6) Cox, R. A.; Patrick, R. *Int. J. Chem. Kinet.* **1979**, *11*, 635.
- (7) Morel, O.; Simonaitis, R.; Heicklen, J. *Chem. Phys. Lett.* **1980**, *73*, 38.
- (8) Graham, R. A.; Winer, A. M.; Pitts, J. N., Jr. *Geophys. Res. Lett.* **1978**, *5*, 909.
- (9) Molina, L. T.; Molina, M. J. *J. Photochem.* **1981**, *15*, 97.
- (10) Singer, R. J.; Crowley, J. N.; Burrows, J. P.; Schneider, W.; Moortgat, G. K. *J. Photochem. Photobiol.* **1989**, *48*, 17-32.
- (11) MacLeod, H.; Smith, G. P.; Golden, D. M. *J. Geophys. Res.* **1988**, *93*, 3813-3823.
- (12) Donaldson, D. J.; Frost, G. J.; Rosenlof, K. H.; Tuck, A. F.; Vaida, V. *Geophysical Research Letters* **1997**, *24*, 2651-2654.
- (13) Zhang, H.; Roehl, C. M.; Wennberg, P. O. paper presented at the AEAP conference, Snowmass Colorado, 2000.
- (14) Wennberg, P. O.; Salawitch, R. J.; Donaldson, D. J.; Hanisco, T. F.; Lanzendorf, E. J.; Perkins, K. K.; Lloyd, S. A.; Vaida, V.; Gao, R. S.; Hints, E. J.; Cohen, R. C.; Swartz, W. H.; Kusterer, T. L.; Anderson, D. E. *Geophysical Research Letters* **1999**, *26*, 1373-1376.
- (15) Fono, L.; Donaldson, D. J.; Proos, R. J.; Henry, B. R. *Chemical Physics Letters* **1999**, *311*, 131-138.

- (16) Zhang, H.; Roehl, C. M.; Sander, S. P.; Wennberg, P. O. *J. Geophys. Res.*, *accepted for publication* **2000**.
- (17) Mazely, T. L.; Friedl, R. R.; Sander, S. P. *Journal of Chemical Physics* **1994**, *100*, 8040-8046.
- (18) Mazely, T. L.; Friedl, R. R.; Sander, S. P. *J. Phys. Chem.* **1995**, *99*, 8162-8169.
- (19) Mazely, T. L.; Friedl, R. R.; Sander, S. P. *J. Phys. Chem.* **1997**, *101*, 7090-7097.
- (20) Kenley, R. A.; Trevor, P. L.; Lan, B. Y. *J. Am. Chem. Soc.* **1981**, *103*, 2203.
- (21) May, R. D.; Friedl, R. R. *Journal of Quantitative Spectroscopy & Radiative Transfer* **1993**, *50*, 257-266.
- (22) Hojer, S.; May, R. D.; Miller, C. E. *Journal of Quantitative Spectroscopy & Radiative Transfer* **1996**, *55*, 273-278.
- (23) Li, Z.; Friedl, R. R.; Moore, S. B.; Sander, S. P. *J. Geophys. Res.* **1996**, *101*, 6795-6802.
- (24) *Handbook of Chemistry and Physics*; 71st ed.; Lide, D. R., Ed.; CRC Press: Boca Raton, 1990.
- (25) Watts, J. D.; Gauss, J.; Bartlett, R. J. *Journal of Chemical Physics* **1993**, *98*, 8718-8733.
- (26) Dunning, T. H. *Journal of Chemical Physics* **1989**, *90*, 1007-1023.
- (27) Werner, H. J.; Knowles, P. J. *J. Chem. Phys.* **1985**, *82*, 5053-5063.
- (28) Knowles, P. J.; Werner, H. J. *Chemical Physics Letters* **1985**, *115*, 259-267.
- (29) Werner, H. J.; Knowles, P. J. *J. Chem. Phys.* **1988**, *89*, 5803-5814.
- (30) Knowles, P. J.; Werner, H. J. *Chemical Physics Letters* **1988**, *145*, 514-522.
- (31) Saxon, R. P.; Liu, B. *Journal of Physical Chemistry* **1985**, *89*, 1227-1232.
- (32) Chen, Z.; Hamilton, T. P. *Journal of Physical Chemistry* **1996**, *100*, 15731-15734.
- (33) Jitariu, L. C.; Hirst, D. M. *Journal of Physical Chemistry A* **1999**, *103*, 6673-6677.

Table 1. Measurement Conditions and Results for 248 nm PNA Photolysis Experiments.

Pressure Torr	Flow Rate sccm	no. of measurements	Slope	[PNA] 10¹³ molecule cm⁻³	[HNO₃] 10¹⁴ molecule cm⁻³
3.0	500	13	14.4	2.6-31	4.9-36
	700-900	8	11.4	1.4-12	1.8-23
7.0	500	17	8.3	2.3-41	7.7-81
	700-1400	10	16.6	7.7-29	4.2-23
10.0	500	5	5.3	4.6-14	6.9-21
	700-900	7	9.2	14-43	5.9-17

Table 2. Electronic Configurations of HO₂NO₂ Singlet and Triplet States

State	Electronic Configuration
1 ¹ A	(core) ¹⁰ (1-17)a ² 18a ² 19a ² 20a ² 21a ⁰ 22a ⁰ 23a ⁰
2 ¹ A	20a → 21a
3 ¹ A	19a → 21a
1 ³ A	18a → 21a
2 ³ A	20a → 21a

Table 3. Vertical Excitation Energies (VEEs), in eV.

State	CASSCF	MRCI
	VEE(cc-pVDZ)	VEE(cc-pVDZ)
1 ¹ A	0.0	0.0
2 ¹ A	4.78	5.05
3 ¹ A	5.41	5.52
1 ³ A	4.03	4.26
2 ³ A	4.57	4.76

Table 4. Optimized Geometries for the Ground and Lowest Triplet State of HO₂NO₂. Bond lengths in Å, Angles in deg., Energy in hartrees.

Parameters	CCSD(T)/cc-pVDZ	
	Ground State	Lowest Triplet State
NO	1.200	1.292
NO'	1.200	1.294
NO''	1.518	1.515
OO''	1.418	1.427
OH	0.975	0.976
∠ONO	133.6	108.7
∠O'NO	109.9	108.9
∠OON	108.1	104.4
∠HOO	101.6	100.7
∠OO'NO	-12.2	-53.7
∠HOON	84.2	82.2
Energy	-355.19609	-355.08444

Figure Captions

Figure 1. Diagram of the experimental apparatus. Details of the optical configuration of the detection axis are presented in the text.

Figure 2. NO₂ LIF signals (arbitrary units) from the photolysis of PNA. Fluorescence from background NO₂, excimer laser-induced cell fluorescence and probe laser scatter have been subtracted from the temporal profiles. For the three experiments shown, the concentrations of PNA and the Ar buffer gas pressures were: a) 3.4×10^{13} molecule cm⁻³ and 3.0 Torr, b) 9.5×10^{13} molecule cm⁻³ and 7.0 Torr, and c) 1.9×10^{14} molecule cm⁻³ and 10.0 Torr. The signal rise observed in a) and b) is due to collisional energy transfer from high vibrational levels of the X(²A₁) state of NO₂¹⁷.

Figure 3. Plot of the ratios of NO₂ fluorescence from back-to-back 248 nm photolysis experiments using HNO₃ and HO₂NO₂ as a function of the corresponding relative concentrations of each precursor. The circles, squares, triangles indicate data obtained at 3.0, 7.0, and 10.0 Torr total pressure, respectively.

Figure 4. Optimized structure of HO₂NO₂.

Figure 5. Potential energy curves of HO₂NO₂ in the Franck-Condon region along the O-O' (a), N-O' (b) and N-O' (c) coordinates.

